Blood Ties: Co_3O_4 Decorated Blood Derived Carbon as a Superior Bifunctional Electrocatalyst

*Chao Zhang, Markus Antonietti, and Tim-Patrick Fellinger**

A simple, versatile and cheap synthetic route is demonstrated for the preparation of Co_3O_4 decorated blood powder derived heteroatom doped porous carbon (BDHC). The inorganic hybrid performs well as an advanced bifunctional non-precious metal electrocatalyst. The hybridization of Co_3O_4 with the blood-derived carbon results in improved activities not only towards the oxygen reduction reaction (ORR), but also in the reverse oxygen evolution reaction (OER). An improved ORR activity and a tuned four electron transfer selectivity can be assigned to a synergistic catalytic effect due the intimate contact between Co_3O_4 particles and the highly conductive heteroatom doped carbon support, mediated by cobalt-nitrogen or cobalt-phosphorous coordination sites. This heterojunction may facilitate the electron transfer by preventing an accumulation of electron density within the Co_3O_4 particles. The straight-forward and cheap synthesis of the highly active and durable electrocatalyst make it a promising candidate for a next-generation bifunctional electrocatalyst for applications such as reversible fuel cells/electrolyzers or metal air batteries.

1. Introduction

The ever-increasing sustainable energy demands have drawn a great deal of interest to electrochemical energy conversions and/or storage technologies.[1] To meet the growing global requirements in terms of energy conversion and distribution, the exploration of alternative electrodes with a controlled chemical composition and well-designed architecture will be an ongoing task to achieve a dramatic performance enhancement.[2] We also need to keep in mind the use of abundant resources to guarantee recyclability and low costs, which further challenges the current research. The electrochemical conversion of the O^{2-}/oxygen couple is the heart of the next-generation energy technologies including metal-air batteries and devices, which can be reversibly used as water electrolyzer and fuel cell, both with a desired zero emission regarding greenhouse gasses. The oxygen reduction reaction (ORR) is the ubiquitous cathode reaction in fuel cells, while the oxygen evolution reaction (OER) is the anode reaction employed in energy conversion and storage such as electrolysis cells, solar fuel synthesis and rechargeable metal-air batteries.[3] However, the sluggish kinetics in the electrocatalytic reduction and evolution of molecular oxygen severely limit the efficiency of these devices.[3a,4]

A large range of materials has been explored in order to find an efficient and stable electrocatalyst for the critical oxygen side. Even the more promising materials still show multiple problems in performance. Platinum (Pt), which is commercially used as ORR catalyst in form of carbon-supported Pt nanoparticles (Pt/C) suffers from the cross-over effect and low durability.[5] Iridium oxide (IrO_2) and ruthenium oxide (RuO_2) are regarded as the most promising OER electrocatalyst in acid and base, respectively. Both catalysts show good efficiency and high current densities at low overpotentials, but also lack in long-term stability. In addition to the performance problems, so far these most promising catalysts are not viable, because of the low abundance and very high costs.[6] Over recent years, considerable research efforts have been made to the design and synthesis of the OER electracatalyst based on earth-abundant elements.[7] To achieve practical applications, earth-abundant cobalt oxides or substituted cobaltites exhibit relatively good OER activities.[7,8] On the other hand, carbon nanomaterials, due to their high stability, conductivity and the possibility to control the morphology, are very interesting materials and already widely applied in electrochemical devices e.g., as catalyst support in polymer-electrolyte fuel cells.[1b,9] Heteroatom doping here can further improve bulk properties and surface chemical properties. Highly interesting observations like synergistic catalytic effects (due to dyade formation)[4b,9,10] on the catalytic activity of hybrid carbon materials but also on the direct electrocatalytic activity of e.g., heteroelements doped carbon[2a,4d,11] towards the ORR can be attributed to this. Moreover, in many examples it has been possible to synthesize carbons and carbon hybrids from renewable precursors and in an environmentally friendly process.[12] Hybrid materials have been proposed to further promote the electrocatalytic activity of the as-obtained materials.[2a,10e,11a,13] Therefore, the development of sustainable and efficient bifunctional O^{2-}/oxygen electrocatalysts from cheap and abundant materials is highly desired for a successful future of fuel cells and metal air batteries.[14]

Recent research shows that the preparation of doped carbons have moved from expensive, and (or) hazardous organic chemicals to renewable biomass as precursors due to the sustainable considerations. Some efforts have been taken to synthesize

Dr. C. Zhang, Prof. M. Antonietti, Dr. T.-P. Fellinger
Max-Planck Institute of Colloids and Interfaces
Am Mühlenberg 1
14476, Potsdam, Germany
E-mail: Tim.Fellinger@mpikg.mpg.de

DOI: 10.1002/adfm.201402770

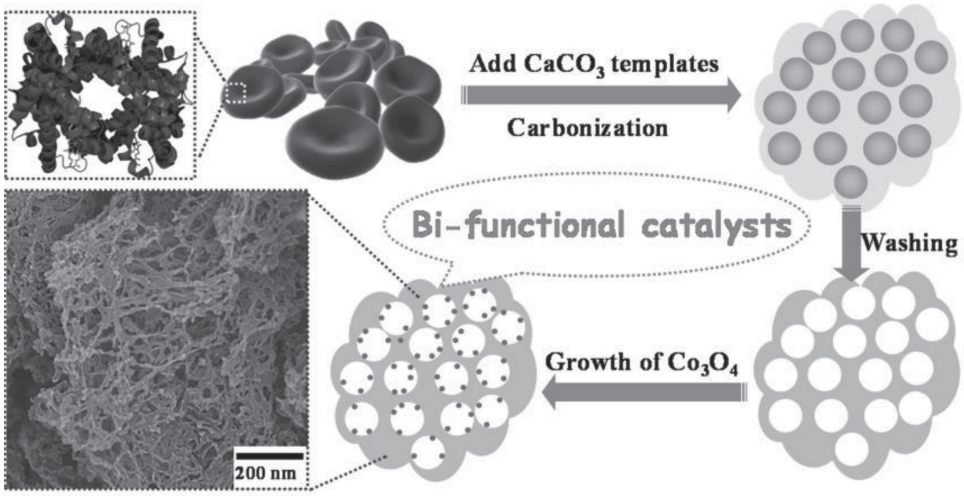

Scheme 1. Schematic of the fabrication process for Co_3O_4 decorated BDHC.

porous carbons from organic-rich bio-wastes such as prawn shells, pig bones, egg-shell membranes and human hairs.[15] Herein, we present a simple strategy that enables facile, economical and scalable preparation of foam-like porous heteroatom doped carbon/Co_3O_4 nanoparticle hybrid materials. First the foam-like heteroatom doped carbon is obtained from a concerted hard templating and activation strategy using conventional blood powder (BP) as a carbon source and commercial $CaCO_3$ nanoparticles as template and activating agent (**Scheme 1**). Nanosized $CaCO_3$ templates are commercially available and very cheap, with a particle size that can be well-tuned in the range of 10–100 nm with a narrow distribution. Compared with the previous silica and soft template methods, the $CaCO_3$ template method is more facile and cost-efficient. However, up to date, only few kinds of precursors such as sucrose, polyacrylonitrile, phenol-formaldehyde (PF) resin, melamine-formaldehyde (MF) resin, and gelatin were utilized using $CaCO_3$ templates for the synthesis of porous carbons.[16] Different from other precursors, herein BP was chosen as unique carbon precursor for the synthesis of nitrogen, phosphorus and sulfur ternary-doped porous carbon. Different from other reports, which used solution-based methods to homogeneously disperse $CaCO_3$ templates within the precursor matrix we simply used a solid state grinding technique to successfully homogenate precursor and template before carbonization. In a second step Co_3O_4 nanoparticles were deposited onto the blood powder derived heteroatom doped carbon (BDHC) by a simple one-pot thermal deposition technique.

2. Results and Discussion

The as-received BP, which is derived from drying pig's blood, is a widely used fertilizer and in large amounts cheap commercially available source of protein with excellent crude protein values and a typical elemental composition of 50 wt% carbon, 15 wt% nitrogen, 0.5 wt% sulfur, and 6 wt% hydrogen.[17] Thus, BP may be considered as a promising and sustainable precursor for heteroatom-doped carbons (with heteroatoms being especially nitrogen, but also sulfur and phosphorous).[18] It is to mention that of course other heteroatoms, such as sulfur and oxygen, but also phosphorous coming from protein and nucleic acids will be incorporated to certain content. Especially in the context of ORR, where Fe-N coordinated macrocylcles are expected to present highly active catalytic sites,[4a,9c] BP is attractive due to presence of large amounts[17] of heme complexes, which give rise to the red-brown color of BP. Most of the blood protein appears in blood cells which have –depending on the type of cell- spherical or plate-like shapes (Figure S1a). The utilization of nanosized $CaCO_3$ with a particle size of *circa* 23 nm (Figure S1b) as a hard template/activating agent, it is interesting to find that highly porous BDHCs with variable morphologies can be obtained simply by changing the initial mass ratios of BP to $CaCO_3$. As investigated by electron microscopy, for the initial ratio of BP:$CaCO_3$ = 2/1, the as-prepared carbon, namely, BDHC-2:1, has large interconnected mesopore system with a typically spherical pore shape and pores being similar to the particle size of the used $CaCO_3$ nanospheres. This clearly indicates the partial shape replication by means of nanocasting, i.e., that the $CaCO_3$ particles were embedded into the precursor matrix to act as hard templates for the mesopore generation (**Figure 1**a,b and Figure S1c). When the relative amount of $CaCO_3$ was increased (BP:$CaCO_3$ = 1:1) a highly porous carbon (BDHC-1:1) with a foam-like morphology, composed of a fibrous network was found (Figure 1c, d and Figure S1d). For comparison, the carbonization of BP without $CaCO_3$ template, further denoted as BCNC, created carbons with smooth surfaces, indicating no obvious porosity throughout the sample (Figure S1e). It should be noted that nanosized $CaCO_3$ template is not only very cheap; it can also very easily be removed with diluted hydrochloric acid. This is a clear advantage over traditional silica hard templating, which often has to be removed by corrosive hydrofluoric acid.[19] Interestingly, in spite of the complicated structure of BP, the template can easily be dispersed within the carbon matrix by simple, but thorough grinding, as evidenced by SEM imaging of BP-$CaCO_3$ mixture after grinding (Figure S1f).

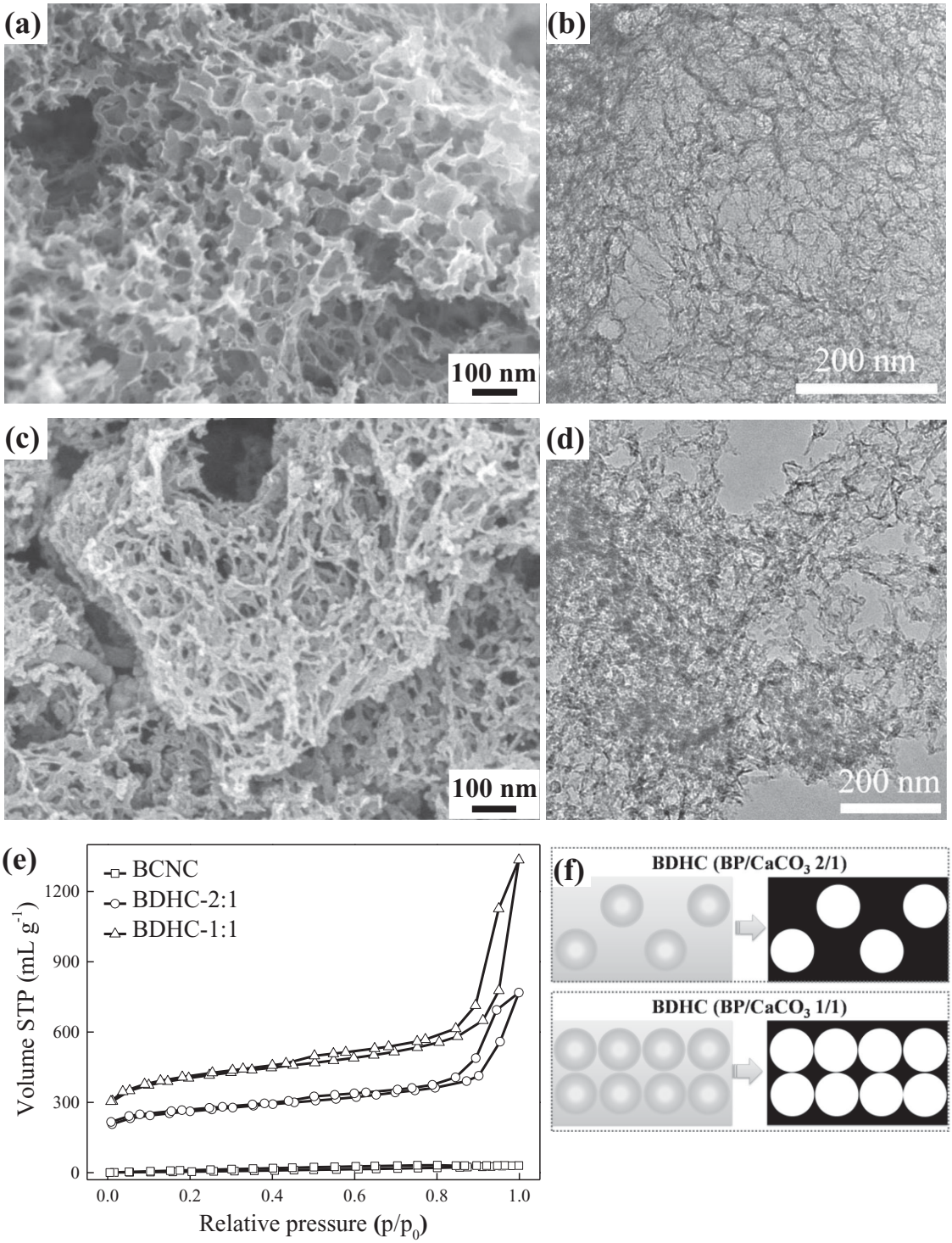

Figure 1. SEM and TEM images of a, b) BDHC-2:1 and c, d) BDHC-1:1, respectively. e) Nitrogen sorption isotherms of BCNC, BDHC-2:1 and BDHC-1:1. f) Schematic representation of the formation of BDHC from the $CaCO_3$-templating methods.

Nitrogen sorption analysis was performed to get a more detailed insight into the products porosity. Apparent surface areas (**Table 1**) and pore size distributions (Figure S2) of BDHCs were determined by the typical nitrogen (77 K) adsorption/desorption isotherms (Figure 1f) by applying the Brunauer-Emmett-Teller (BET) model and the nonlocal density functional theory (NLDFT) equilibrium model method for slit pores, respectively. The templated BDHCs (BDHC-1:2 and BDHC-1:1) show nitrogen (77 K) adsorption/desorption isotherms similar to IUPAC type IV, with a sharp capillary

Table 1. Composition and nitrogen sorption data of BCNC, BDHC, Co_3O_4@BDHC and Co_3O_4.

Sample	Elemental analysisa [wt%]				S_{BET} [m^2 g^{-1}]	Pore volume [mL g^{-1}]		
	N	S	C	H		Total	Micro	Meso
BCNC	2.9	0.2	87.0	1.9	34	0.04	0	0.04
BDHC-2:1	2.8	0.2	84.7	1.8	825	0.84	0.22	0.62
BDHC-1:1	2.9	0.2	84.2	1.7	1288	1.14	0.34	0.80
Co_3O_4@BDHC1	2.4	0.2	64.5	1.7	1137	1.60	0.35	1.25
Co_3O_4@BDHC2	1.9	0.1	45.5	1.5	495	1.08	0.09	0.99
Co_3O_4@BDHC3	1.1	0.1	23.4	1.2	159	0.45	0.02	0.43
Co_3O_4	0	0	0	0	180	0.22	0	0.22

a)The elemental composition was evaluated using a combustion method.

condenzation step at very high relative pressures ($p/p_0 > 0.9$) and an H1-type hysteresis loop, indicating the existence of large pores in the as-prepared material.[20] However, there is also hysteresis in the medium high pressure range ($0.45 < p/p_0 < 0.8$), indicative of mesopore contribution. At low relative pressures ($p/p_0 < 0.1$), strong micropore contributions can be observed, depending on the amount of $CaCO_3$ used. The increase of the initial BP:$CaCO_3$ ratio dramatically increases the nitrogen adsorption volume, indicating an additional activating role of the $CaCO_3$. In agreement with the electron microscopical observations and in contrast to BDHC-2:1 and BDHC-1:1, BCNC shows a negligible amount of nitrogen adsorption, indicating a very low surface area. The overall specific surface areas significantly increase from BCNC (34 m^2 g^{-1}), due to the concerted $CaCO_3$ templating and activation to 825 and 1288 m^2 g^{-1} for the BDHC-2:1 and BDHC-1:1, respectively. Interestingly, there is no clear maximum in the pore size distribution at 23 nm, i.e., at the size of the hard template. Also there is no increase in the contribution of pores with this diameter at higher fractions of $CaCO_3$. We cannot observe a one-to-one replication of the template structure. However, the foam-like character can be explained by a strong contribution of gas evolution to the pore formation process. This obviously goes along with the amount of $CaCO_3$ and points to the additional role as activating agent.

To investigate the carbonization process to form BDHCs, thermogravimetric analysis (TGA) up to 1000 °C was carried out in N_2 atmosphere (Figure S2a). It can be seen, that neat $CaCO_3$ powder decomposes at about 600 °C, and a large weight loss can be observed between 600 and 760 °C. The characteristic thermogram can be explained by the thermal decomposition of $CaCO_3$ into calcium oxide and CO_2.[16a,21] The main carbonization process (accompanied by mass loss) of neat BP occurs at the temperature range 240 to 800 °C. For the $CaCO_3$ templated samples, the weight loss of the sample still continues at the temperature range 800 to 900 °C, indicating that the CO_2 derived from the pyrolysis of $CaCO_3$ may react with the carbon components, which will further induce the weight loss of the carbon samples. Therefore, during the carbonization process, the $CaCO_3$ particles not only serve as a hard template for producing mesopores, but also offer CO_2 which can act as activation agent to create micropores, by means of the Boudouard equilibrium, at temperature higher than the $CaCO_3$ pyrolysis temperature. Physical activation of carbon with CO_2 is also an effective method to prepare activated carbon materials. However, the method has its inevitable disadvantages when it was used to prepare doped porous carbons for the applications as an electrocatalyst. Firstly, physical activation with CO_2 is usually conducted at certain temperatures (typically at ~700–900 °C depending on different carbon sources), however, in this study, to increase the graphitization effect (influencing the conductivity of the as-obtained carbons) and control the content of heteroelements within the as-obtained carbons (influencing the active sites for the electrocatalytic performance), a tedious and high-energy-consuming two-step heat treatment is unavoidable. In this study, during the carbonization process, nanosized $CaCO_3$ templates decomposed and in situ released CO_2 to develop micropores, and mesopores were generated by subsequent acid removal of the as-formed CaO nanoparticles.

Figure 1f proposes a possible mechanism for the formation of fibrous network structures of the BDHC-1:1 sample. The large amounts of $CaCO_3$ templates within precursor matrix are inclined to percolate, and thus interconnected cavity channels may form during the carbonization process of the BP followed by the removal of templates. The X-ray diffraction (XRD) patterns of BP, $CaCO_3$ and BDHCs (before and after washing with acid) are shown in Figure S4. BP gives a XRD pattern with typical protein semi-crystalline peaks located at ca. 9° and 21° originated from triple-helical and adjacent protein strands.[22] The BDHCs show a broad diffraction peak centered at ~24.3°, indicating the existence of amorphous carbon after the carbonization of BP, and the peaks centered at ca. 31.8° and 46.3° correspond to reflections of the (200) and (220) planes of NaCl, respectively (JCPDS, No. 72–1668), which is the main impurity in the raw BP. Besides, the peak centered at ca. 45° corresponds to the (200) planes of α-Fe (JCPDS, No. 87–0722), indicating the carbonization of hemoglobin in BP produces materials containing iron species in the form of α-Fe. After aqueous acidic washing, the peaks ascribed to NaCl and α-Fe disappear, indicating successful removal of the impurities from the as-prepared samples.

In order to immobilize homogeneously distributed Co_3O_4 onto BDHCs, wet-chemistry methods (see experimental part) were utilized here to obtain highly porous Co_3O_4@BDHC hybrid materials. Unless not explicitly noted, in the following BDHC-1:1 was used as supporting material. The series of Co_3O_4@BDHC hybrids are denoted as Co_3O_4@BDHC1,

Co_3O_4@BDHC2 and Co_3O_4@BDHC3, respectively, with the increasing content of Co_3O_4 in the Co_3O_4@BDHC hybrid. Wide-angle X-ray diffraction (WAXD) was used to study the composition of Co_3O_4@BDHC1, Co_3O_4@BDHC2 and Co_3O_4@BDHC3 (**Figure 2**a). The neat BDHC displays a broad diffraction peak centered at $2\theta = 24.3°$, being characteristic for amorphous carbons. All the sharp diffraction peaks of the Co_3O_4 sample can be indexed with crystal planes of the cubic phase of Co_3O_4 (JCPDS, No. 74–2120). Although these peaks are not apparent in Co_3O_4@BDHC1 due to the low content of Co_3O_4 in this hybrid, the XRD patterns of Co_3O_4@BDHC2 and Co_3O_4@BDHC3 clearly confirm the successful deposition of Co_3O_4 onto the BDHC. Based on the TGA analysis of BDHC, Co3O4@BDHC1, Co3O4@BDHC2, Co3O4@BDHC3 and Co3O4 in an air atmosphere, the contents of Co3O4 in Co3O4@BDHC1, Co3O4@BDHC2 and Co3O4@BDHC3 can be calculated to be about 7 wt%, 27 wt% and 48 wt%, respectively. X-ray photoelectron spectroscopy (XPS) was carried out to investigate elemental composition and binding motifs. The atomic percentages of carbon, oxygen, cobalt, nitrogen, phosphorous, and sulfur are estimated as 66%, 20%, 5%, 3.4%, 3.4%, 1%, respectively. Therefore XPS further confirms the nitrogen doping in the Co_3O_4@BDHC2. Figure 2b presents the high-resolution N1s spectrum fitted into two peaks at 398.3 and 400 eV, which correspond with pyridinic and pyrrolic nitrogen, respectively.[12g] The XPS N1s peak at 398.3 eV could be also assigned to a cobalt–nitrogen related bond, which is the bonding between the pyrrolic nitrogens and the cobalt ions.[23]

From the C1s spectra and curve fits of Co_3O_4@BDHC2 (Figure S5a), four peaks centered at 284.5, 286, 287.9 and 289.8 eV are observed, corresponding with C-C, C-O (C-N or C-S), C = O (or C = N) groups, respectively.[12g] The Co2p spectrum (Figure S5b) exhibit two strongest peaks at 780.7 and 796.4 eV correspond to $Co2p_{3/2}$ and $Co2p_{1/2}$, respectively. The $Co2p_{3/2}$ spin-orbital component has a weak satellite located about 5.3 eV above the main peak, and all the results confirm the formation of the Co_3O_4 phase.[13c,24] Two kinds of Co bond configurations that are Co(II)O (779.4 eV) and Co(II)Nx (780.5 eV) are observed (see inset in Figure S5b).[25] The result indicates that Co(II)Nx bonding configuration is successfully introduced during the in situ growth of cobalt oxides, and this likely plays an important role in improving the electrocatalytic activity. Due to similar electronegativity of O, P and S the Co(II)O peak may be overlapped by Co-S or Co-P contributions. The impact of sulfur is considered to be comparably low, whereas the high contents of nitrogen and phosphorus may contribute to the formation of cobalt-nitrogen and cobalt-phosphorous coordination sites, respectively. In the high-resolution O1s region (Figure S5c), the Co_3O_4@BDHC2 display three oxygen peaks. The peak at 531.4 eV is typically due to cobalt-oxygen bonds, and they are usually associated with oxygen in OH groups, indicating that the surface of the Co_3O_4@BDHC2 is hydroxylated to some extent as a result of either surface oxyhydroxide or the substitution of oxygen atoms at the surface by hydroxyl groups.[13c] The lower peak (~530 eV) could be assigned to the lattice oxygen species O^{2-}. The component at 533.5 eV can be attributed to physi- and chemisorbed water at the surface.

Electron micrographs of Co_3O_4@BDHC1, Co_3O_4@BDHC2, Co_3O_4@BDHC3 and Co_3O_4 (Figure S6 and Figure S7) show that all hybrids retain the general BDHC-1:1 morphology of the fibrous network after the growth of Co_3O_4 onto the carbon substrate. No visible Co_3O_4 particles were found in the Co_3O_4@BDHC1 both in the SEM and TEM images, while Co_3O_4 nanoparticles with a size of <10 nm and 20–40 nm were found for

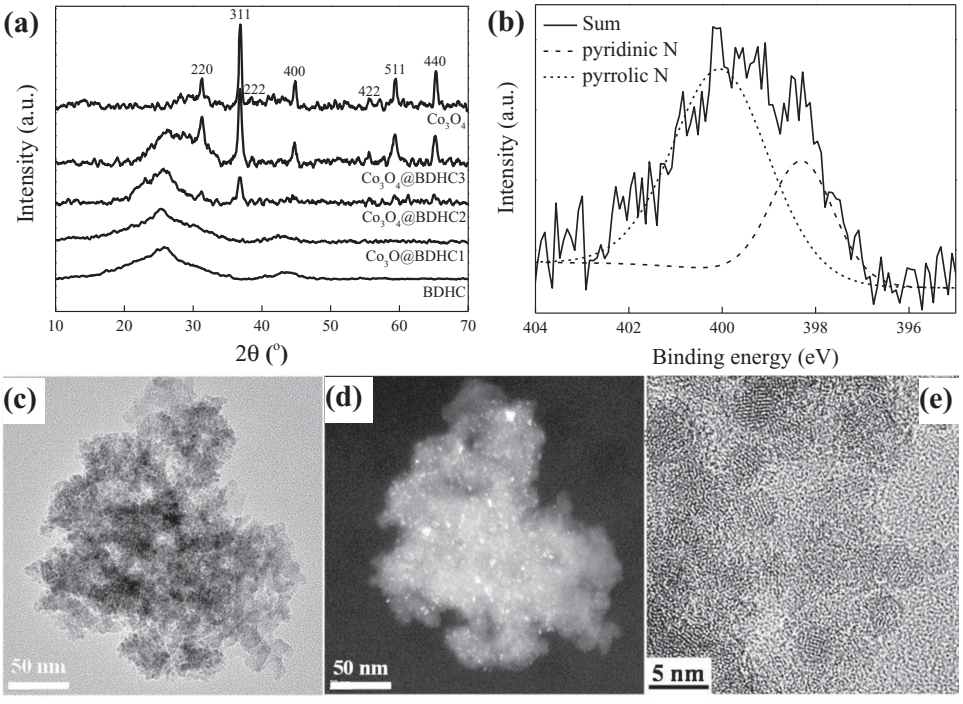

Figure 2. a) WAXD curves of BDHC, Co_3O_4@BDHC and Co_3O_4. b) High resolution N1s spectra of Co_3O_4@BDHC2. c) Bright-field and d) dark field TEM images of Co_3O_4@BDHC2. e) High-resolution TEM image of Co_3O_4@BDHC2.

Co_3O_4@BDHC2 and Co_3O_4@BDHC3, respectively. Figure 2c,d shows bright-field and dark-field TEM images recorded on the same area of Co_3O_4@BDHC2 sample. As can be seen in the dark-field image, the Co_3O_4 nanoparticles with bright contrast are uniformly embedded in the continuous foam-like carbon matrix. The high-resolution TEM image of Co_3O_4@BDHC2 sample (Figure 2e) clearly confirmed that the highly crystalline Co_3O_4 nanoparticles were well-dispersed, not agglomerated, and nearly monodisperse, with a mean particle size of 3 ± 1 nm in the amorphous carbon matrix. The small particle size indicates the tendency of Co_3O_4 to be deposited onto the surface of the BDHC in form of small metal oxide clusters or nanoparticles depending on the concentration of the Co precursors. Apparently, the heteroatom doped carbon surface efficiently acts as high surface area nucleation site for the particle formation leading to well-dispersed nanoparticles.

To evaluate the final porosity of the hybrid materials, nitrogen sorption analysis was performed. Isotherms and pore size distributions of BDHC, Co_3O_4@BDHChybrid materials and neat Co_3O_4 are summarized in Table 1. As shown in Figure S8a, all samples still show the sharp capillary condenzation step at high relative pressures. More importantly, successively reduced micropore contributions are observed for the Co_3O_4 decorated samples with increasing amounts of Co_3O_4 (Figure S8c and Table 1). It can be concluded that either Co_3O_4 nanoparticles grow within the carbon micropores or at least block the pores, which is more likely considering the spherical shape of the particles. In any case, this observation hints to a homogeneous distribution of Co_3O_4 within the BDHC. Generally, with increasing amount of metal oxide the values of specific surface areas and pore volumes decrease simply because of the additional high density material.[26] However, it should be underlined, that the important mass transport meso- and macropore structure is retained and is of great importance for favorable kinetics in electrocatalytic reactions.

To investigate the electrochemical oxygen reduction performance for the Co_3O_4@BDHC hybrid materials, cyclic voltammograms (CV) in 0.1 M KOH, either saturated with N_2 (dotted line) or O_2 (solid line) were measured. In the presence of oxygen, additional cathodic peaks, being indicative of ORR activity, can be observed for all BDHC and BDHC hybrids (**Figure 3**a). For the bare BDHC catalyst we observe a single cathodic reduction peak at 0.64 V vs RHE. Interestingly, the lower Co_3O_4 decorated carbon hybrids Co_3O_4@BDHC1 and Co_3O_4@BDHC2 show slightly positively shifted ORR peak potentials both at 0.73 V vs RHE. However, a negative shift to 0.60 V vs RHE is observed at higher Co_3O_4 concentration of Co_3O_4@BDHC3. For comparison, the neat Co_3O_4 electrode (mixed with 20 wt% conductive carbon black additive[27]) shows the cathodic reduction peak at 0.60 V vs RHE. These results clearly indicate a significant enhancement in the ORR electrocatalytic activity for the hybridization of BDHC and Co_3O_4 with a proper ratio, i.e., Co_3O_4 particle size and/or coverage.

The linear sweep voltammetry (LSV) measurements on a rotating disk electrode (RDE) for each of the electrode materials (including commercial Pt/C and IrO_2 reference electrocatalysts) in O_2-saturated 0.1 M KOH electrolytes at a scan rate of 10 mV/s and a rotation rate of 1600 rpm were then conducted (Figure 3b). The respective LSVs at different rotation rates can be found in the SI (Figure S10). Among the as-prepared samples, the Co_3O_4@BDHC2 electrocatalyst was more active for the ORR than the bare BDHC and Co_3O_4 samples, indicating greatly enhanced activities for ORR due to the synergistic effect of Co_3O_4 intimately bound to BDHC. Although the commercial Pt/C catalyst shows a more positive onset potential than Co_3O_4@BDHC hybrid materials, the Co_3O_4@BDHC2 electrocatalyst exhibits only ~50 mV cathodic shift at the half-wave potential compared to the Pt/C electrocatalyst. Especially the IrO_2 reference catalyst (excellent OER electrocatalyst) with strongly negative shifted onset potential and largely decreased limiting current density cannot be considered as a good ORR catalyst i.e., is not an option as a bifunctional catalyst for running reactions reversibly. It should be mentioned that for BDHC, Co_3O_4@BDHC1, Co_3O_4@BDHC2 and the Pt/C reference, limiting current densities in the range of the theoretical Levich current (at a rotating rate of 1600 rpm) are observed. This indicates a proper thin film coating, but also a selective four electron process at least at high polarization. The neat Co_3O_4 sample, which had a promising peak position in the CV curves, here shows strongly reduced performance and a much lower limiting current density indicating a low selectivity towards the four electron mechanism. Interestingly, we can find a similar behavior for the case of Co_3O_4@BDHC3, which might be a hint on a high coverage of the more ORR active BDHC with Co_3O_4.

The as-prepared Co_3O_4/BDHC mixture electrode shows a negative shift of the half-wave potential by ~18 mV as compared to the Co_3O_4@BDHC2 hybrid and similar limiting current density (Figure 3c). However, the overall performance is much better than that of the neat Co_3O_4 sample with commercial carbon additive. This clearly indicates an enhanced catalytic activity caused by the intimate contact of the Co_3O_4 nanoparticles with the more ORR active carbon support and the main contribution coming from the BDHC, which seems to be activated by the cobalt oxide.

The corresponding Koutecky-Levich (K-L) plots (J^{-1} vs $\omega^{-1/2}$) of the Co_3O_4@BDHC2 electrode at various electrode potentials showed good linearity (Figure 3d). The slopes remain approximately constant over the potential range, which suggests that the electron transfer numbers for oxygen reduction at different electrode potentials are similar. The linearity and parallelism of the plots is an indication of first-order reaction kinetics with respect to the concentration of dissolved O_2. The electrons transfer number in the ORR process for the Co_3O_4@BDHC2 electrode is found to be above 3.93 from 0.69 to 0.80 V, suggesting that the Co_3O_4@BDHC hybrids favor a 4e oxygen reduction process, similar to ORR catalyzed by a high-quality commercial Pt/C catalyst.

The electron transfer number of carbon-based materials sometimes strongly depends on the mass loading on the disk electrode. The ORR performance of the Co3O4@BDHC hybrid electrodes with different catalyst loadings (56, 140, 280, 420 and 560 μg cm^{-2}) on the glassy carbon, and the electron transfer numbers are evaluated for comparison. The effect of different catalyst loadings is demonstrated in Figure S12a. Changing the catalyst loading from high loading, i.e., 560 μg cm^{-2}, to lower loading, the diffusion limited current initially remains constant at ~6 mA cm^{-2}, but drops significantly once the loading

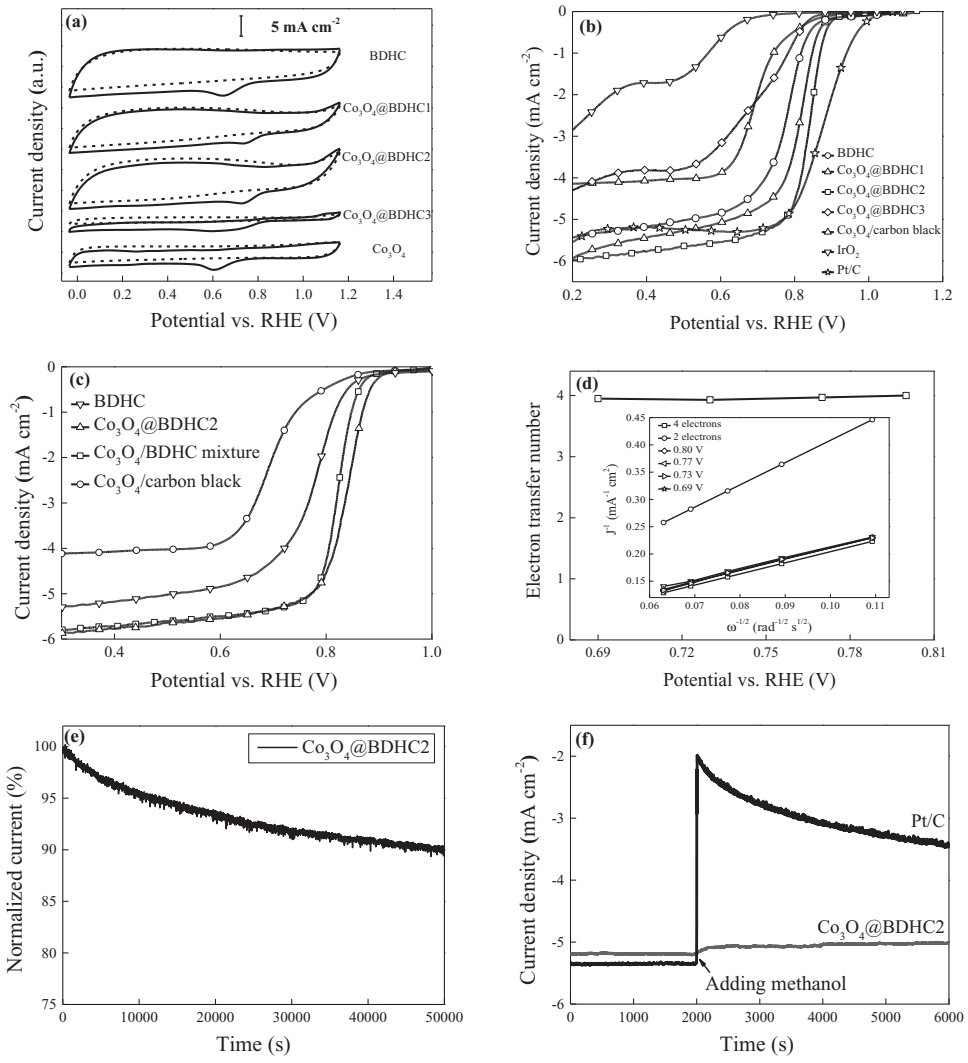

Figure 3. a) CV curves of BDHC, Co_3O_4@BDHC hybrid materials and Co_3O_4 in N_2-saturated (dash line) or O_2-saturated (solid line) 0.1 M KOH. b) RDE polarization curves of BDHC, Co_3O_4@BDHC hybrid materials, IrO_2 and Pt/C in O_2-saturated 0.1 M KOH with a sweep rate of 10 mV s^{-1}, 1600 rpm. c) Comparison of the RDE polarization curves of BDHC, Co_3O_4@BDHC2, Co_3O_4/BDHC mixture and Co_3O_4 in O_2-saturated 0.1 M KOH with a sweep rate of 10 mV s^{-1}, 1600 rpm. d) Dependence of electron transfer numbers on potentials of Co_3O_4@BDHC2 electrodes. Inset is the K-L plots of Co_3O_4@BDHC2 electrodes at various potentials. e) Durability of Co_3O_4@BDHC2 at 0.76 V in O_2-saturated 0.1 M KOH, 1600 rpm. f) Chronoamperometry responses of Co_3O_4@BDHC2 and Pt/C at 0.76 V in O_2-saturated 0.1 M KOH with 1 M methanol, 1600 rpm.

is decreased below 140 μg cm^{-2} (Figure S13b). The reason for this is that the low amount of supported catalyst is no longer capable of spreading completely over the whole surface of the glassy carbon support. Accordingly the electrons transfer numbers in the ORR process for the Co3O4@BDHC2 electrode decrease with decreasing catalyst loadings (Figure S12c). If the limiting current density cannot be reached anymore we also cannot apply K-L analysis properly, therefore the lower electron transfer numbers are artefacts of the low coverage. At very high loading of 560 μm cm^{-2} two reasons may lead to the obviously wrong value of 4.54 electrons. First the slope in the kinetically limited region of the polarization curve is so high, that the error of the datapoint selected for K-L analysis is very high. Second the high loading may lead to a film thickness, which is too high, i.e., the catalyst is invading the diffusion layer of the disk electrode, changing the mass transport characteristics, which are crucial for the K-L analysis.

Furthermore, the durability of Co_3O_4@BDHC2 catalysts toward ORR was tested by performing chronoamperometric measurements at 0.76 V vs RHE (Figure 3e). Here Co_3O_4@BDHC2 presents better durability with only ~10% reduced current density after ~14 hours. Furthermore and in contrast to the Pt/C reference, the cobalt oxide-BDHC hybrid presents excellent resistance towards the methanol crossover effect, which is one of the main challenges faced by the Pt-based catalysts in fuel cells (Figure 3f).[5]

To evaluate the catalytic activity of the hybrid materials for reverse reaction, which is the oxygen evolution reaction (water splitting) we also measured voltammetry at high potentials (up to 1.75 V vs RHE) in the same electrolytes (0.1 M KOH).

Typically, the catalytic OER activity of Co_3O_4 is attributed to the redox reactions between the Co(II), Co(III) and Co(IV) species on the surface of the sample (Figure S13).[28] This surface redox reactivity can be probed by the CV curves in a potential window slightly lower than the OER onset potentials.[29] CV curves were measured at 2 mV s^{-1} and compared for the bare BDHC, Co_3O_4@BDHC2 and neat Co_3O_4 electrodes (**Figure 4**a). Measurements performed at different scan rates can be found in SI (Figure S14). Bare BDHC shows a typical double-layer capacitive behavior and no obvious redox features can be observed in the potential window of 0.71–1.56 V vs RHE. The Co_3O_4@BDHC hybrids clearly show three anodic peaks (A1, A2 and A3) and three cathodic peaks (C1, C2 and C3). Due to literature peaks A1 and A2 correspond to the oxidation of Co(II) to hydrous Co(III) and dispersed Co(III), respectively, and the A3 peak to the oxidation of Co(III) to Co(IV).[28b,29,30] As we cannot observe a clear A3 peak due to further increasing anodic current, we conclude significant oxygen evolution currents to overlap the A3 peak, which counts for the Co^{+4} species to act as the active catalytic center. This interpretation goes along with other reports on spinel cobaltite phases by several researchers.[28c,31]

The oxygen evolution activities of the Co_3O_4@BDHC hybrid materials were further investigated and compared to bare BDHC-1:1, neat Co_3O_4 and the IrO_2 and Pt/C reference catalysts by LSV measurements in 0.1 M KOH (scan speed: 10 mV/s; potential range: 1.45–1.75 V; Figure 4b). To compare the catalysts we evaluate the overpotential at 10 mA cm^{-2} current density and denote it as η_{10}; a characteristic value, which was recently suggested to benchmark OER catalysts by Jamarillo et al.[6b] No oxygen evolution current was found on the bare BDHC-1:1 electrode in the applied potential range, indicating first, that the heteroatom-doped porous carbon shows low catalytic activity towards OER and second, oxidation stability at potentials up to 1.75 vs RHE. Very weak OER performance was also detected in the Pt/C sample, showing that the excellent ORR catalyst Pt/C is not suitable as a bifunctional electrocatalyst for both OER and ORR. As a high performance OER standard IrO_2 shows a very low onset potential and an η_{10} of 1.59 V. These characteristics prove the very high OER activity, however going along with very low ORR activity and high costs. For the bare Co_3O_4 standard (again with 20 wt% conductive carbon black additive[32]) the onset potential is strongly shifted to more positive potentials and η_{10} is 1.66 V. If we compare the performance with the Co_3O_4@BDHCs performances, we can observe the following trends. All three hybrid materials outperform the neat Co_3O_4 catalyst in both onset potential and η_{10}. Co_3O_4@BDHC1 only shows partially better properties, as the onset potential is more negative and η_{10} is at low 1.65 V vs RHE, but at higher overpotentials the current densities are outperformed by the neat Co_3O_4. Co_3O_4@BDHC2 and Co_3O_4@BDHC3 have very low onset potentials as well as very low η_{10} values of 1.61 and 1.59 V vs RHE, respectively (Figure 3). The overpotentials with regard to the thermodynamic water oxidation potential are therefore only 420, 380 and 360 mV for Co_3O_4@BDHC1, Co_3O_4@BDHC2 and Co_3O_4@BDHC3. Like for the ORR performance evaluation the assumed positive effect of the in situ growing of Co_3O_4 onto the BDHC was further studied by comparison of the best bifunctional hybrid catalyst Co_3O_4@BDHC2 with the mechanic mixture of Co_3O_4

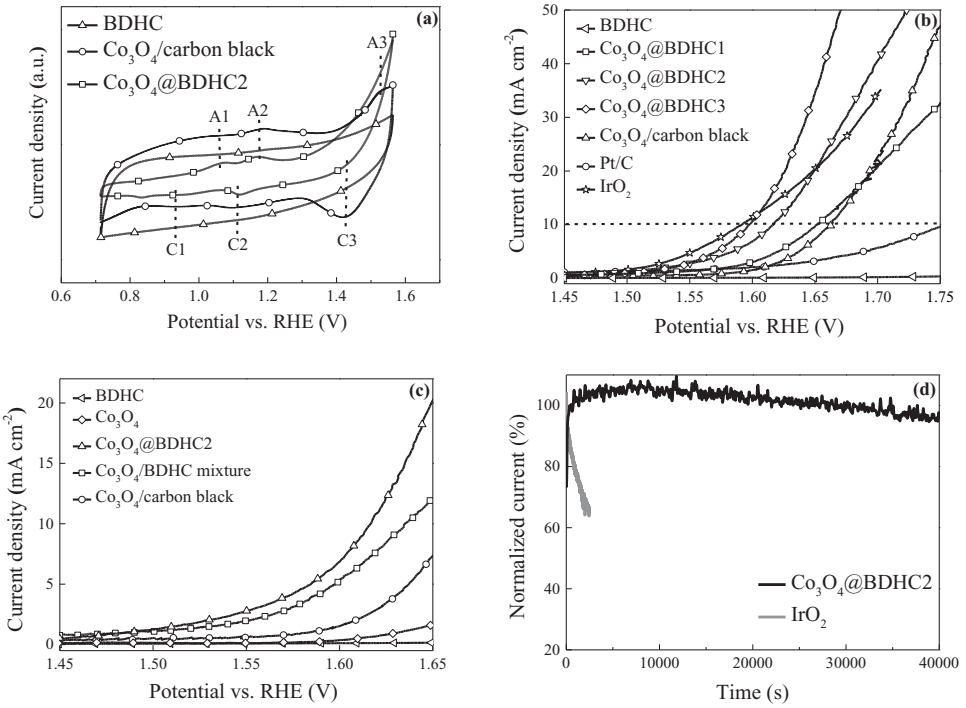

Figure 4. a) Comparison of CV curves of BDHC, Co_3O_4@BDHC2 and Co_3O_4 in 0.1 M KOH with a sweep rate of 2 mV s^{-1}. b) LSV curves of BDHC, Co_3O_4@BDHC hybrid materials, Co_3O_4, Pt/C and IrO_2 measured in N_2-saturated 0.1 M KOH with a sweep rate of 10 mV s^{-1}, 1600 rpm. c) Comparison of the LSV curves of BDHC, Co_3O_4@BDHC2, Co_3O_4/BDHC mixture, Co_3O_4 with and without carbon black in N_2-saturated 0.1 M KOH with a sweep rate of 10 mV s^{-1}, 1600 rpm. d) Durability of Co_3O_4@BDHC2 and commercial IrO_2 at a current density of 10 mA cm^{-2} in 0.1 M KOH, 1600 rpm.

and BDHC-1:1 in equivalent mass ratios. For comparison the polarization curves of Co_3O_4/BDHC mixture are presented as well (Figure 4c). Like in the ORR study, we can again observe a strongly increased catalytic activity of the hybrid material as compared to the simple mixture. Obviously, the intimate contact in between the cobalt oxide and the BDHC has a crucial role in forming the promising bifunctional catalyst. At the OER side this can easily be understood by reduced electron transfer resistance, however an additional synergistic effect (e.g., by dyade formation) like observed at the ORR side cannot be excluded. The OER performance of the Co_3O_4/BDHC mixture is better than that of the neat Co_3O_4/carbon black electrode, which can be explained by stronger improved interfaces between BDHC support and the OER active cobalt oxide. These statements are confirmed by impedance measurements, which can be found in SI (Figure S16). Tafel plots of LSVs are derived and shown in Figure S17, from which small Tafel slopes down to 47 and 53 mV/dec were found for Co_3O_4@BDHC2 and Co_3O_4/carbon black, respectively, at lower overpotentials. It should be noted that the Tafel slope of the Co_3O_4/BDHC mixture sample increases to 51 mV per decade, which indicates that the charge transfer within the Co_3O_4/BDHC mixture sample is better than that of Co_3O_4/carbon black for the OER.

The ORR and OER performances of crude BP is also tested and compared (Figure S18). We can clearly see that the blood powder electrode shows much weaker ORR and OER performance compared with the Co_3O_4@BDHC2 electrode, indicating the essential of the hybridization of Co_3O_4 and blood derived carbon for the high-performance ORR and OER bifunctional catalyst. However, the reader should recognize the oxidation stability of the doped carbon at high potentials.

The capacitances vs potential and Mott-Schottky plots were determined for Co_3O_4@BDHC2 at different frequencies, respectively (Figure S19), and it was found that the Co_3O_4 within Co_3O_4@BDHC2 behaves like a p-type semiconductor over the frequency ranges in KOH electrolytes.[33] It was evident that the value of capacitance rises rather sharply in the potential window, which can be ascribed to the increasing specific adsorption of OH^- ions on the electrode surface. The maximum capacitance at ~1.21 V lies near the A2 voltammetric peak potential and thus may be assigned to the oxidation of Co(II) to Co(III) process.[33] Due to their near-metallic character, carbon materials usually take the role of the metal. However, nitrogen and phosphorus, when doped into carbon, may act as electron donors thus tuning the position of the valence band or conduction band of the doped carbon phase, resulting in an altered work function and sometimes a slightly opened band gap.[34] Different from the carbon-Co_3O_4 contact, once the band gap of the heteroelement doped carbon is opened, the BDHC-Co_3O_4 contact could also promote Mott-Schottky effects and change both the electronic structure of Co_3O_4 and BDHC, which is beneficial for activating the performance of the hybrid than that of neat Co_3O_4 by increasing their electron density.[35]

Besides the high electrocatalytic OER activity of the as-prepared Co_3O_4/BDHC hybrid materials, a long-term chronoamperometric stability test in 0.1 M KOH at η_{10} further indicates an excellent stability of the most promising bifunctional hybrid catalyst Co_3O_4/BDHC2 (Figure 4f). Running Co_3O_4/BDHC2 ~11 hours at η_{10}, i.e., at 380 mV overpotential, after an initial activation leads to an activity loss of only 4%, whereas the IrO_2 standard is very sensitive to alkaline conditions, loosing ~35% activity already after 42 minutes. The chronoamperometric test impressively shows the high durability of the as-prepared Co_3O_4/BDHC hybrid catalysts towards OER.

3. Conclusion

In conclusion we have demonstrated the design and fabrication of sponge-like blood-derived heteroatom doped carbon-supported Co_3O_4 as an efficient bifunctional electrochemical catalyst, processing an outstanding activity and performance towards both ORR and OER in alkaline conditions. The optimized bifunctional shows a half wave potential of 0.83 V vs RHE at the ORR side and a characteristic overpotential of only 380 mV at 10 mA cm^{-2} at the OER side. The very cheap and facile synthesized catalysts therefore gives comparable performances to commercial Pt/C catalyst at the ORR side and at the same time comparable results to IrO_2 catalyst at the OER side. The additional high durability in alkaline conditions, make this distinguished material a promising candidate as O^{2-}/oxygen electrocatalyst for reversible fuel cells/electrolyzers and/or metal-air batteries. The unique fibrous network structure of the blood-derived heteroatom doped carbon comes from the concerted hard templating and activation using $CaCO_3$ nanoparticles. The high surface area and strongly heteroatom doped material features stable anchoring sites for the immobilization of Co_3O_4, which greatly reduce aggregation and growth of the decorated Co_3O_4 nanoparticles and improve the charge transfer between the two species. Additionally, the intimate contact of the carbon scaffold and the cobalt oxide, leads to a synergistic catalytic effect at least at the ORR side. Here the ORR activity of the heteroatom doped carbon is clearly improved by Co_3O_4 decoration. At the OER side the improved activity may be explained already by the improved conductivity of the Co_3O_4 due to the attachment to the carbon, however the strong performance improvement indicates a synergistic effect also for the anode reaction.

4. Experimental Section

Materials and Methods: Blood powder was used as received via eBay from a German slaughterhouse. Nanosized $CaCO_3$ with a diameter of 23 nm (BET surface area: 69.9 m^2/g) were purchased from Solvay Chemicals (Infra Bad Hönningen GMBH, Germany). All the other reagents were purchased from Sigma-Aldrich and used without further purification. Deionized (DI) water was used throughout the experiments. Blood-derived heteroatom doped carbon (BDHC) was prepared with a BP-to-$CaCO_3$ mass ratio of 2 and 1, respectively. In a typical synthesis a mixture of 100 mg of BP and designed amounts of $CaCO_3$ template was grounded using a mortar for 5 min. The mixture was transferred into a crucible and heated to 900 °C (5 °C min^{-1}) with a dwelling time of 2 hours in a N_2 atmosphere Nabertherm N 11/H oven. The as-prepared products were washed with excess 1 M HCl and dried at 50 °C overnight in vacuo. Co_3O_4 decorated BDHC were prepared as follows: in a typical experiment, 50 mg of BDHC as the starting material, was dispersed in an appropriate amount of ethanol solution of $Co(NO_3)_2 \cdot 6\ H_2O$ by sonication for 5 min. After drying at 80 °C to remove the solvent, the obtained precursor mixture, i.e., $Co(NO_3)_2$ infiltrated BDHC material, was calcined at 400 °C for 2 h in air. For the sake of brevity, the obtained hybrid material are denoted as Co_3O_4@BDHC. By controlling the initial

mass ratios of BDHC and $Co(NO_3)_2 \cdot 6\ H_2O$, the Co_3O_4@BDHC hybrid was fabricated with three different theoretical BDHC/Co_3O_4 mass ratios: Co_3O_4@BDHC1 (BDHC/Co_3O_4 = 50 mg/10 mg), Co_3O_4@BDHC2 (BDHC/Co_3O_4 = 50 mg/15 mg) and Co_3O_4@BDHC3 (BDHC/Co_3O_4 = 50 mg/20 mg). For comparison, bare Co_3O_4 was also prepared using the same procedure in the absence of BDHC.

Characterization: Elemental analysis for carbon, hydrogen, nitrogen and sulfur was accomplished using combustion analysis by a Vario Micro device. SEM images were obtained on a JEOL JSM-7500F microscope with a 15 kV accelerating voltage. The C1s, N1s and Co2p survey spectra were recorded using a Thermo Scientific K-Alpha instrument using Monochromatic X-ray source Al Kα (1486.6 eV). TEM measurements were performed on bright and dark modes using a Zeiss EM 912Ω instrument. XRD patterns were measured on a Bruker D8 Advance instrument using Cu-Kα radiation (λ = 1.5418 Å). Nitrogen sorption testings were measured at 77 K in a N_2 atmosphere after degassing the samples at 150 °C under vacuum for 10 hours using a Quantachrome Quadrasorb SI porosimeter. The apparent surface area was calculated by applying the Brunauer-Emmett-Teller (BET) model to the isotherm data points of the adsorption branch in the relative pressure range $p/p_0 < 0.3$. The pore size distribution was calculated from nitrogen sorption data using the nonlocal density functional theory (NLDFT) equilibrium model method for slit pores provided by Quantachrome data reduction software QuadraWin Version 5.11. TGA measurements were carried out on a Netzsch TG 209 F1 device under constant N_2 flow with a heating rate of 5 °C min^{-1}.

Electrochemical Measurements: The electrocatalytic activity of all samples for the ORR and OER performance was tested in a conventional three-electrode cell using a Reference 600 potentiostat/galvanostat equipped with a RDE 710 Rotating Electrode setup (Gamry Instruments, Inc.). The catalyst ink was prepared by adding 5 mg of catalyst powder into a mixture solution of 95 µl of 5% Nafion solution and 350 µl of ethanol. After sonication for 30 min, 5 µl of catalyst ink was deposited onto 5 mm diameter polished glassy carbon electrode (Gamry Instruments, Inc.) and dried at room temperature. The catalyst loadings were calculated to be 0.28 mg cm^{-2} for all the tests. The same loadings of commercial 20 wt% Pt/C catalyst (Alfa Aesar) and IrO_2 were used as a reference. The rotating disk electrode (RDE) measurements were conducted in N_2- and O_2-saturated 0.1 M KOH using the Ag/AgCl (in saturated aq. KCl) electrode as the reference electrode and a platinum wire as the counter electrode. More detailed descriptions for the electrochemical measurements can be found in the SI.

Supporting Information

Supporting Information is available from the Wiley Online Library or from the author.

Acknowledgements

The authors acknowledge the technical staff for performing numerous service measurements throughout the research. The authors also acknowledge the striking spirit at Air France. Costs caused by this are the reason for our figures to appear only in greyscale. Thanks!

Received: August 13, 2014
Revised: September 19, 2014
Published online: October 18, 2014

[1] a) M. Gao, W. Sheng, Z. Zhuang, Q. Fang, S. Gu, J. Jiang, Y. Yan, *J. Am. Chem. Soc.* **2014**, *136*, 7077–7084; b) L. Dai, D. W. Chang, J. B. Baek, W. Lu, *Small* **2012**, *8*, 1130–1166; c) P. V. Kamat, G. C. Schatz, *J. Phys. Chem. C* **2009**, *113*, 15473–15475.

[2] a) Y. Li, W. Zhou, H. Wang, L. Xie, Y. Liang, F. Wei, J. C. Idrobo, S. J. Pennycook, H. Dai, *Nat. Nanotechnol.* **2012**, *7*, 394–400; b) J. Jiang, Y. Li, J. Liu, X. Huang, C. Yuan, X. W. Lou, *Adv. Mater.* **2012**, *24*, 5166–5180; c) Z. S. Wu, Y. Sun, Y. Z. Tan, S. Yang, X. Feng, K. Mullen, *J. Am. Chem. Soc.* **2012**, *134*, 19532–19535; d) D. W. Wang, F. Li, M. Liu, G. Q. Lu, H. M. Cheng, *Angew. Chem. Int. Ed.* **2008**, *47*, 373–376.

[3] a) Y. Gorlin, T. F. Jaramillo, *J. Am. Chem. Soc.* **2010**, *132*, 13612–13614; b) V. Nikolova, P. Iliev, K. Petrov, T. Vitanov, E. Zhecheva, R. Stoyanova, I. Valov, D. Stoychev, *J. Power Sources* **2008**, *185*, 727–733; c) T. Maiyalagan, K. A. Jarvis, S. Therese, P. J. Ferreira, A. Manthiram, *Nat. Commun.* **2014**, *5*, 3949; d) Y. Shao, F. Ding, J. Xiao, J. Zhang, W. Xu, S. Park, J.-G. Zhang, Y. Wang, J. Liu, *Adv. Funct. Mater.* **2013**, *23*, 987–1004.

[4] a) M. Winter, R. J. Brodd, *Chem. Rev.* **2004**, *104*, 4245–4270; b) M. Lefevre, E. Proietti, F. Jaouen, J. P. Dodelet, *Science* **2009**, *324*, 71–74; c) M. G. Walter, E. L. Warren, J. R. McKone, S. W. Boettcher, Q. Mi, E. A. Santori, N. S. Lewis, *Chem. Rev.* **2010**, *110*, 6446–6473; d) K. Gong, F. Du, Z. Xia, M. Durstock, L. Dai, *Science* **2009**, *323*, 760–764.

[5] Y. Bing, H. Liu, L. Zhang, D. Ghosh, J. Zhang, *Chem. Soc. Rev.* **2010**, *39*, 2184–2202.

[6] a) L. Duan, F. Bozoglian, S. Mandal, B. Stewart, T. Privalov, A. Llobet, L. Sun, *Nat. Chem.* **2012**, *4*, 418–423; b) C. C. McCrory, S. Jung, J. C. Peters, T. F. Jaramillo, *J. Am. Chem. Soc.* **2013**, *135*, 16977–16987.

[7] a) M. Grzelczak, J. Zhang, J. Pfrommer, J. Hartmann, M. Driess, M. Antonietti, X. Wang, *ACS Catalysis* **2013**, *3*, 383–388; b) P. Du, R. Eisenberg, *Energ. Environ. Sci.* **2012**, *5*, 6012.

[8] a) S. Singh, *Int. J. Hydrogen. Energ* **1996**, *21*, 171–178; b) P. Nkeng, *J. Electrochem. Soc.* **1995**, *142*, 1777.

[9] a) F. Jaouen, S. Marcotte, J.-P. Dodelet, G. Lindbergh, *J. Phys. Chem. B* **2003**, *107*, 1376–1386; b) U. A. Paulus, A. Wokaun, G. G. Scherer, T. J. Schmidt, V. Stamenkovic, V. Radmilovic, N. M. Markovic, P. N. Ross, *J. Phys. Chem. B* **2002**, *106*, 4181–4191; c) G. Wu, K. L. More, C. M. Johnston, P. Zelenay, *Science* **2011**, *332*, 443–447.

[10] a) S. Yun, H. Zhang, H. Pu, J. Chen, A. Hagfeldt, T. Ma, *Adv. Energy Mater.* **2013**, *3*, 1407–1412; b) J. Duan, Y. Zheng, S. Chen, Y. Tang, M. Jaroniec, S. Qiao, *Chem. Commun.* **2013**, *49*, 7705–7707; c) H. Wang, H. Dai, *Chem. Soc. Rev.* **2013**, *42*, 3088–3113; d) S. Pylypenko, S. Mukherjee, T. S. Olson, P. Atanassov, *Electrochim. Acta* **2008**, *53*, 7875–7883; e) Y. Liang, Y. Li, H. Wang, J. Zhou, J. Wang, T. Regier, H. Dai, *Nat. Mater.* **2011**, *10*, 780–786.

[11] a) P. Chen, T. Y. Xiao, Y. H. Qian, S. S. Li, S. H. Yu, *Adv. Mater.* **2013**, *25*, 3192–3196; b) S. Chen, J. Bi, Y. Zhao, L. Yang, C. Zhang, Y. Ma, Q. Wu, X. Wang, Z. Hu, *Adv. Mater.* **2012**, *24*, 5593–5597, 5646; c) Q. Li, R. Cao, J. Cho, G. Wu, *Adv. Energy Mater.* **2014**, *4*, n/a-n/a; d) J. Liang, Y. Zheng, J. Chen, J. Liu, D. Hulicova-Jurcakova, M. Jaroniec, S. Z. Qiao, *Angew. Chem. Int. Ed.* **2012**, *51*, 3892–3896; e) Z. Wen, S. Ci, Y. Hou, J. Chen, *Angew. Chem. Int. Ed.* **2014**, *53*, 6496–6500.

[12] a) H. Bi, Z. Yin, X. Cao, X. Xie, C. Tan, X. Huang, B. Chen, F. Chen, Q. Yang, X. Bu, X. Lu, L. Sun, H. Zhang, *Adv. Mater.* **2013**, *25*, 5916–5921; b) B. Hu, K. Wang, L. Wu, S. H. Yu, M. Antonietti, M. M. Titirici, *Adv. Mater.* **2010**, *22*, 813–828; c) M. M. Titirici, M. Antonietti, *Chem. Soc. Rev.* **2010**, *39*, 103–116; d) R. J. White, N. Yoshizawa, M. Antonietti, M.-M. Titirici, *Green Chem.* **2011**, *13*, 2428; e) N. Baccile, M. Antonietti, M. M. Titirici, *ChemSusChem* **2010**, *3*, 246–253; f) T.-P. Fellinger, R. J. White, M.-M. Titirici, M. Antonietti, *Adv. Funct. Mater.* **2012**, *22*, 3254–3260; g) S.-A. Wohlgemuth, R. J. White, M.-G. Willinger, M.-M. Titirici, M. Antonietti, *Green Chem.* **2012**, *14*, 1515; h) Y. Fang, D. Gu, Y. Zou, Z. Wu, F. Li, R. Che, Y. Deng, B. Tu, D. Zhao, *Angew. Chem. Int. Ed.* **2010**, *49*, 7987–7991.

[13] a) Z. Yang, M. Liu, C. Zhang, W. W. Tjiu, T. Liu, H. Peng, *Angew. Chem. Int. Ed.* **2013**, *52*, 3996–3999; b) G.-L. Tian, Q. Zhang, B. Zhang, Y.-G. Jin, J.-Q. Huang, D. S. Su, F. Wei, *Adv. Funct. Mater.* **2014**, n/a-n/a; c) Z. Zhao, H. Wu, H. He, X. Xu, Y. Jin, *Adv. Funct. Mater.* **2014**, *24*, 4698–4705.

[14] a) L. Jörissen, *J. Power Sources* **2006**, *155*, 23–32; b) F. Cheng, J. Chen, *Chem. Soc. Rev.* **2012**, *41*, 2172–2192; c) N. S. Choi, Z. Chen, S. A. Freunberger, X. Ji, Y. K. Sun, K. Amine, G. Yushin, L. F. Nazar, J. Cho, P. G. Bruce, *Angew. Chem. Int. Ed.* **2012**, *51*, 9994–10024.

[15] a) L. Wang, Y. Zheng, X. Wang, S. Chen, F. Xu, L. Zuo, J. Wu, L. Sun, Z. Li, H. Hou, Y. Song, *ACS Appl. Mater. Interfaces* **2014**, *6*, 7117–7125; b) L. Yang, A. Zhang, X. Zheng, *Energ. Fuel.* **2009**, *23*, 3859–3865; c) W. Qian, F. Sun, Y. Xu, L. Qiu, C. Liu, S. Wang, F. Yan, *Energ. Environ. Sci.* **2014**, *7*, 379; d) Z. Li, L. Zhang, B. S. Amirkhiz, X. Tan, Z. Xu, H. Wang, B. C. Olsen, C. M. B. Holt, D. Mitlin, *Adv. Energy Mater.* **2012**, *2*, 431–437; e) W. Huang, H. Zhang, Y. Huang, W. Wang, S. Wei, *Carbon* **2011**, *49*, 838–843; f) H. Liu, Y. Cao, F. Wang, W. Zhang, Y. Huang, *Electroanal.* **2014**, *26*, 1831–1839.

[16] a) C. Zhao, W. Wang, Z. Yu, H. Zhang, A. Wang, Y. Yang, *J. Mater. Chem.* **2010**, *20*, 976; b) B. Xu, L. Peng, G. Wang, G. Cao, F. Wu, *Carbon* **2010**, *48*, 2377–2380; c) Y. Mao, H. Duan, B. Xu, L. Zhang, Y. Hu, C. Zhao, Z. Wang, L. Chen, Y. Yang, *Energ. Environ. Sci.* **2012**, *5*, 7950; d) G. Yang, H. Han, T. Li, C. Du, *Carbon* **2012**, *50*, 3753–3765; e) X. Y. Chen, C. Chen, Z. J. Zhang, D. H. Xie, X. Deng, *Ind. Eng. Chem. Res.* **2013**, *52*, 10181–10188.

[17] The elemental composition was evaluated using a combustion method.

[18] S. Satoh, A. Hernández, T. Tokoro, Y. Morishita, V. Kiron, T. Watanabe, *Aquaculture* **2003**, *224*, 271–282.

[19] B. Xu, S. Hou, F. Zhang, G. Cao, M. Chu, Y. Yang, *J. Electroanal. Chem.* **2014**, *712*, 146–150.

[20] W. Li, D. Chen, Z. Li, Y. Shi, Y. Wan, G. Wang, Z. Jiang, D. Zhao, *Carbon* **2007**, *45*, 1757–1763.

[21] H. Liu, C.-Y. Cao, F.-F. Wei, Y. Jiang, Y.-B. Sun, P.-P. Huang, W.-G. Song, *J. Phys. Chem. C* **2013**, *117*, 21426–21432.

[22] a) A. Fiorani, C. Gualandi, S. Panseri, M. Montesi, M. Marcacci, M. L. Focarete, A. Bigi, *J Mater Sci Mater Med* **2014**; b) K. Okuyama, *Connect. Tissue Res.* **2008**, *49*, 299–310.

[23] a) K. Lee, L. Zhang, H. Lui, R. Hui, Z. Shi, J. Zhang, *Electrochim. Acta* **2009**, *54*, 4704–4711; b) T. Okada, *J. Electrochem. Soc.* **1998**, *145*, 815; c) G. Faubert, G. Lalande, R. Côté, D. Guay, J. P. Dodelet, L. T. Weng, P. Bertrand, G. Dénès, *Electrochim. Acta* **1996**, *41*, 1689–1701.

[24] V. M. Jiménez, A. Fernández, J. P. Espinós, A. R. González-Elipe, *J. Electron Spectrosc.* **1995**, *71*, 61–71.

[25] a) H. Wang, X. Bo, A. Wang, L. Guo, *Electrochem. Commun.* **2013**, *36*, 75–79; b) H.-C. Huang, I. Shown, S.-T. Chang, H.-C. Hsu, H.-Y. Du, M.-C. Kuo, K.-T. Wong, S.-F. Wang, C.-H. Wang, L.-C. Chen, K.-H. Chen, *Adv. Funct. Mater.* **2012**, *22*, 3500–3508.

[26] T. C. Chou, R. A. Doong, C. C. Hu, B. Zhang, D. S. Su, *ChemSusChem* **2014**, *7*, 841–847.

[27] The positive effect ofthe addition of conductive additive can be found in SI (Figure S15).

[28] a) M. E. G. Lyons, M. P. Brandon, *Int. J. Electrochem. Sci.* **2008**, *3*, 1425–1462; b) M. E. G. Lyons, M. P. Brandon, *J. Electroanal. Chem.* **2010**, *641*, 119–130; c) S. Palmas, F. Ferrara, A. Vacca, M. Mascia, A. M. Polcaro, *Electrochim. Acta* **2007**, *53*, 400–406.

[29] J. A. Koza, Z. He, A. S. Miller, J. A. Switzer, *Chem. Mater.* **2012**, *24*, 3567–3573.

[30] N. Spataru, C. Terashima, K. Tokuhiro, I. Sutanto, D. A. Tryk, S. M. Park, A. Fujishima, *J. Electrochem. Soc.* **2003**, *150*, E337–E341.

[31] R. N. Singh, *J. Electrochem. Soc.* **1990**, *137*, 1408.

[32] The positive effect ofthe addition of conductive additive can be found in SI (Figure S11).

[33] N. Fradette, *J. Electrochem. Soc.* **1998**, *145*, 2320.

[34] a) Y. Zhou, K. Neyerlin, T. S. Olson, S. Pylypenko, J. Bult, H. N. Dinh, T. Gennett, Z. Shao, R. O'Hayre, *Energ. Environ. Sci.* **2010**, *3*, 1437; b) X. H. Li, M. Antonietti, *Chem. Soc. Rev.* **2013**, *42*, 6593–6604.

[35] X. H. Li, J. S. Chen, X. Wang, J. Sun, M. Antonietti, *J. Am. Chem. Soc.* **2011**, *133*, 8074–8077.